Int J Adv Manuf Technol (2009) 45:506–520
DOI 10.1007/s00170-009-1992-0

ORIGINAL ARTICLE

Finite element prediction of material removal rate due to traveling wire electrochemical spark machining

Mohan Charan Panda · Vinod Yadava

Received: 16 September 2008 / Accepted: 20 February 2009 / Published online: 18 March 2009

Abstract Manufacturing engineers are facing new challenges during machining of electrically nonconducting or partially conducting materials such as glass, quartz, ceramics, and composites. Traveling wire electrochemical spark machining (TW-ECSM), a largely unknown technology, has been applied successfully for cutting these types of materials. However, hardly any theoretical work has been reported related to machining performance of TW-ECSM process. The present work is an attempt in this direction. In the present work, a 3-D finite element transient thermal model has been developed to estimate the temperature field and material removal rate (MRR) due to Gaussian distributed input heat flux of a spark during TW-ECSM. First, the developed code calculates the temperature field in the workpiece and then MRR is calculated using this temperature field. The calculated MRR has been compared with the experimental MRR for verifying the approach. Computational experiments have been performed for the determination of energy partition and spark radius of a single spark. The effects of various process parameters such as energy partition, duty factor, spark radius, and ejection efficiency on MRR have been reported. It has been found that MRR increases with increase in energy partition, duty factor, and ejection efficiency but decreases with increase in spark radius.

Keywords Traveling wire electrochemical spark machining (TW-ECSM) · Material removal rate (MRR) · Finite element method (FEM) · Gaussian heat flux distribution

M. C. Panda · V. Yadava (✉)
Mechanical Engineering Department,
Motilal Nehru National Institute of Technology,
Allahabad, Uttar Pradesh 211004, India
e-mail: vinody@mnnit.ac.in

1 Introduction

For realistic progress in industries, advancements in materials should go hand in hand with the advancement of the machining processes. To machine the advanced difficult-to-machine materials, newer machining processes have come forward. Recently, a new trend has been introduced to combine the features of different machining processes. Such machining processes are called as hybrid machining processes (HMPs). HMPs are developed to exploit the advantages of each of the constituent machining process and diminish the disadvantages of each constituent process. It has been observed that sometimes, hybrid machining process enhances the material removal rate (MRR), increases the capabilities of the constituent processes, and widen the area of application of the constituent processes. HMPs also reduce some adverse effects of the constituent processes when they are applied individually.

Electrochemical spark machining (ECSM) is one of the HMPs, which combines the features of electrochemical machining (ECM) and electrodischarge machining (EDM). ECSM has successfully overcome the limitation of electrical conductivity requirement of the workpiece material to be machined by EDM or ECM. Also, the material removal rate by ECSM has been found five and 50 times faster than that of ECM and EDM, respectively, under the same parameter setting [1]. The ECSM process uses electrochemical discharge (ECD) phenomenon for generating heat for the purpose of removing work material by melting and vaporization. This was presented for the first time in 1968 by Kurafuji as "Electrochemical Discharge Drilling" for microholes in glass [2]. Several other names of ECSM are used in literature by different researchers, such as "Electrochemical Arc Machining" by Kubota, "Electro-

chemical Discharge Machining" by Ghosh et al., and "Spark Assisted Chemical Engraving" by Langen et al. [3]. The diversity of names illustrates the complexity of the process

After almost 40 years of its first mention in literature, the basic mechanism of the process is not yet completely understood and is still a matter of research investigations. Various researchers have put forth explanations of ECD phenomenon based on their experimental studies. Basak and Ghosh [4] treated the discharge phenomenon as a switching off process due to bubble bridges. Jain et al. [5] proposed a valve theory where each gas bubble was considered as a valve, which after its breakdown due to high electric field produces discharge in the form of spark. Kulkarni et al. [6] compared electrochemical discharge process with the arc discharge in gases. Wuthrich et al. [7] suggested that the formation of an isolating gas film around the electrode is responsible for electrochemical discharge phenomenon. The mechanism of the formation of the gas film is much debated in literature. Yerokhin et al. [8] claimed that local Joule heating and vaporization of the electrolyte in the vicinity of the electrode is responsible for the gas film formation. Vogt [9] considered that the increasing density of electrochemically formed bubbles and the effect of electrode wettability is the main mechanism of the formation of the gas film. Fascio et al. [10] developed two theoretical models of the spark assisted chemical engraving (SACE) phenomenon. First model, based on percolation theory, predicts the critical parameters (voltage and current). Second model is used to estimate the spark's characteristics (amplitude and duration) and machining depth. Wuthrich et al. [11] developed a SACE setup based on atomic force microscopy and found that the gas film thickness, in which the electrochemical discharges take place, is the main limiting factor. Further, they have investigated that by adding surfactants to the electrolyte, wettability of the tool electrode increases which reduces the gas film thickness. It is observed experimentally that the critical voltage reduces significantly.

ECSM with ECD have been tried in many ways: hole making using sinking tool electrode, hole making using rotating tool electrode, and cutting using wire tool electrode. Accordingly, they are called as sinking ECSM, drilling ECSM, and traveling wire (TW)-ECSM. Success in the application of sinking and drilling ECSM has stimulated interest in studying the prospects of TW-ECSM. In 1985, Tsuchiya et al. proposed TW-ECSM first time for cutting nonconducting materials such as glasses and ceramics and studied further on by Jain et al. and Peng et al. [3]. TW-ECSM is capable to do slicing of large volume of material without the need for costly full-form tool electrodes. Also, complex shapes in the workpiece can be cut by the use of numerically controlled of movement of workpiece. In TW-ECSM configuration, a wire of diameter less than 1 mm moves with speed less than few centimeters per minute through guides.

TW-ECSM or more general ECSM is a largely unknown technology for which scarce literatures are available. Yet, it has not been commercialized but still under laboratory study stage. McGeough and El Hofy [1] carried out experimental studies on the effects of mode of electrolyte flushing, wire erosion, and machining speed on metal removal rate during TW-ECSM. Their recommendation was to use coaxial mode of flushing for maintaining the machining action and its accuracy. Jain et al. [12] carried out experiments on their self developed setup of TW-ECSM for cutting glass epoxy and Kevlar–epoxy composites using NaOH electrolyte. They found that the wire's wear rate and the overcut follow a similar behavior as the machining rate but the wire's wear rate is about two magnitudes smaller than the MRR. It was also found that there was increase in MRR at higher voltage along with the presence of thermal cracks, large heat affected zone, and irregular machined surfaces. They also tried to study the effect of artificially introducing some bubbles into the process during machining and found that the MRR as well as the overcut decreases slightly. Singh et al. [13] attempted to explore the feasibility of using TW-ECSM process for machining of electrically partially conductive materials like lead zirconate titanate and carbon fiber epoxy composites. They found that MRR increases with increase in supply voltage. MRR also increases with increase in concentration of the electrolyte up to around 20 wt.%. Beyond this concentration, it starts decreasing. They also observed that machined surface shows evidence of melting. Large cracks are sometimes observed when the machining is done at higher voltage. However, such cracking is not seen at lower voltage. Peng and Liao [14] verified that TW-ECDM can be applied for slicing mesosize nonconductive brittle materials of several millimeters thick. They have shown that pulsed dc power shows better spark stability and more spark energy than constant dc power. Nesarikar et al. [15] carried out experimental study for the feasibility of TW-ECSM process for precision slicing of thick Kevlar–epoxy composite. They did comparison between the experimental and calculated values of MRR and average diametral overcut with the variations in electrolyte conductivity, applied voltage, and specimen thickness.

Basak and Ghosh [16] developed a theoretical model for the electrochemical discharge machining. The model has capability to predict the characteristics of the material removal rate for varying input parameters and gives similar trend of MRR with the experimental results. Jain et al. [5] developed a 3-D unsteady heat transfer model for the determination of MRR, overcut, and limited depth of cut during sinking ECSM. In their model, random number

generation scheme to locate the spark over the workpiece has been used. They assumed the nature of the spark as prismatic column with square cross section, which is far from real situation. Bhondwe et al. [17] developed a finite element method (FEM)-based axisymmetric thermal model for computation of MRR considering Gaussian distribution profile of spark during sinking ECSM. They applied the model to two types of materials, soda lime glass and alumina, and found that for soda lime glass, workpiece material MRR increases from 10% to 30% electrolyte concentration significantly. Thereafter, the concentration does not play any role to enhance the MRR. However, for alumina, MRR increases with increase in electrolyte concentration. The change in value of MRR for soda lime glass with concentration is more than that of alumina. They also found that with increase in duty factor, MRR increases for both soda lime glass and alumina workpiece material. However, the variation of MRR with duty factor in alumina is found less than that of soda lime glass.

Some literature have been reviewed which are similar to the action of TW-ECSM. Traveling wire electrodischarge machining (TW-EDM) is the most common. Prasad et al. [18] determined 3-D transient temperature distribution in the moving wire during TW-EDM using FDM. The numerically evaluated crater shapes were compared qualitatively with the results of the experiments. Hargrove and Ding [19] developed a FEM-based model for the determination of temperature distribution and thickness of temperature affected layer in the low carbon steel workpiece during wire electrical discharge machining (WEDM). Through minimizing the thickness of the temperature affected layers and satisfying a certain cutting speed, a set of cutting process parameters were determined for workpiece machining. The experimental investigation of the effects of cutting parameters on the thickness of the low carbon steel workpiece surface layers in WEDM was used to validate the simulation results.

Based on the above literature survey, it has been found that the ECSM process in general and the TW-ECSM process in particular have not been commercialized and literature available for this process is still scarce. It has also been observed that no theoretical/numerical study has been reported to date for the prediction of MRR during TW-ECSM. The present work is an attempt in this direction. In this paper, a FEM-based thermal model is developed for the determination of temperature distribution in the workpiece during TW-ECSM. Temperature field in the workpiece is determined considering heat flux magnitude and distribution of spark, pulse time, duty cycle, and energy partition. After calculation of temperature distribution in the workpiece, the isotherms are plotted using SURFER software. Further, isomelts are used to find the volume of the crater formed by single spark in the workpiece. The volume of material removed by all the sparks during travel of the wire is used to calculate MRR. Computational experiments have also been performed to determine energy partition and spark radius. Particular attention has been paid to study the effects of energy partition, duty factor, spark radius and ejection efficiency on MRR for two different types of workpiece materials, mild steel and glass. The present developed model has few similarities with the model developed by Jain et al. [5] but entirely different. The first difference of the present model with the previous model of Jain et al. is that they developed the model for calculation of MRR during *sinking ECSM* whereas the present model is developed for calculation of MRR during *wire ECSM*. Further, they considered the heat flux profile as a prismatic column with square cross section which is far from reality, whereas in the present model, Gaussian distribution heat flux profile of spark is considered.

2 Mathematical modeling

The configuration of a typical TW-ECSM setup is shown in Fig. 1. In TW-ECSM, the hydrogen gas bubbles are formed all along the circumference of the wire electrode. The coalescence of bubbles form a gas film around the wire electrode when the supply voltage reaches a critical value. This gas film isolates the wire electrode from the electrolyte. Electrical discharges in the form of sparks take place in this gas film and machining of material is possible if the workpiece material is kept in the vicinity of the sparking zone. The material removal in TW-ECSM is mainly caused by the melting and vaporization due to heat generated by the spark. It is considered as a thermal phenomenon [3]. The equations used for modeling and simulation of TW-ECSM include governing equation, boundary conditions, and initial condition.

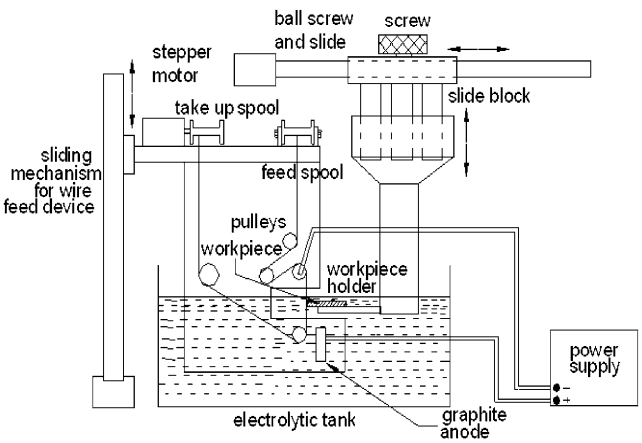

Fig. 1 Configuration of TW-ECSM setup [15]

2.1 Assumptions

To make the analysis of TW-ECSM, mathematically tractable numbers of simplifying assumptions are required to be made, which are written below:

(a) Workpiece material is homogeneous and isotropic. Although the materials used in real practice are not homogeneous in structure, to simplify the problem, it is considered to be homogeneous throughout. Hence, the average values of thermal properties are used.
(b) The thermal properties, viz., specific heat and thermal conductivity, of the workpiece material are treated as temperature independent.
(c) Only a fraction of total spark energy is dissipated as heat into the workpiece. The rest of the heat is assumed to be distributed between the tool and the electrolyte. However, this study is restricted for the prediction of MRR from the workpiece material.
(d) At a time, only one spark is produced at the workpiece top surface (single spark phenomenon) [6] and the duration of spark is same for all discharge.
(e) Shape of heat flux is assumed to be *Gaussian* distributed. From the experimental studies of Kulkarni et al. [6] for single spark, the heat affected zone is circular and the crater is dome shaped. So reflecting the shape of crater, the nature of the heat flux can be approximated as *Gaussian*.
(f) Since the study for the metal removal is carried out for the single spark, to calculate the material removal rate, the sparks occurring per unit time are assumed to be identical.
(g) The energy density of a spark column during the discharge time t_{on} is assumed to be constant.
(h) Ejection efficiency is assumed to be 100%. Also, there is no deposition of recast layer on the machined surface.

2.2 Governing equation

The first step in estimation of MRR is to find the temperature distribution in the workpiece domain. The general 3-D heat diffusion equation within a homogenous and isotropic solid without heat generation in workpiece can be used. This can be written as [20]:

$$k\left[\frac{\partial^2 T}{\partial X^2}+\frac{\partial^2 T}{\partial Y^2}+\frac{\partial^2 T}{\partial Z^2}\right]=\rho C_{\mathrm{p}}\frac{\partial T}{\partial t} \quad \text{in domain} \quad \text{ABCDEFGH} \tag{1}$$

where workpiece-related parameters are density ρ (kg/m^3), specific heat capacity $C_{\mathrm{p}}(J/kg-K)$, and thermal conductivity $k(W/m-K)$. T is temperature in Kelvin and t is time in second. X, Y, and Z are coordinate axes (Fig. 2).

2.3 Initial and boundary conditions

(a) At the start of the TW-ECSM process, the workpiece is immersed in the electrolyte and the temperature of the whole domain is assumed to be at room temperature (T_0), i.e., $T=T_0$ in the workpiece domain ABCDEFGH at $t=0$ (Fig. 2).
(b) The boundaries B_3, B_5, and B_6 of the domain are considered as insulated boundaries (Fig. 2). It is due to the fact that the temperature gradient across these boundaries (B_3, B_5, and B_6) compared to incoming heat flux boundary (B_q) is almost negligible

$$\text{i.e.,}\quad \frac{\partial T}{\partial n}=0 \text{ on } B_3,\ B_5,\ \text{and } B_6 \text{ for } t>0, \tag{2}$$

where n is the outward normal to the boundary.

(c) On the top surface of the domain, the area of B_q receives a total heat Q (from the spark) for a time period t_{on}. After that period, this area receives no heat as the spark moves to another location. Thus,

$$\begin{aligned} q_w &= \tfrac{Q}{B_q} \text{ on area } B_q \text{ for } t\le t_{\mathrm{on}} \\ &= 0 \text{ for } t> t_{\mathrm{on}} \end{aligned} \tag{3}$$

where q_{w} is the heat flux to the workpiece. The expression for q_{w} is given as:

$$q_w(r)=\frac{4.45F_wVI}{\pi R^2}\exp\left\{-4.5\left(\frac{r}{R}\right)^2\right\} \tag{4}$$

where R is spark radius, r is the radial distance from the axis of the spark, V is supply voltage, I is current, and F_{w} is energy partition.

No comprehensive method has so far been proposed to calculate the value of F_{w} during TW-ECSM process. In the present work, F_{w} is taken as 5%. Basak and Ghosh [16] took spark diameter $2a=10^{-6}I_b$, where $2a$ is spark diameter in meters and I_b is the current in amperes at the instant of the circuit opening. But they have assumed that spark channel is cylindrical in shape. Also, Jain et al. [5] assumed prismatic nature of spark with square cross section, which is far from real life situation. Kulkarni et al. [6] gave the crater diameter for different workpiece materials as 300 μm based on their experiments. In the present work, this diameter is taken as spark diameter.

During on time, the remaining area (B_1-B_q) on the top surface of the domain (Fig. 2) losses heat due to convection to the surrounding electrolyte. The area (B_1-B_q) will, however, depend on the location of the discharge. Also, during off time, the whole top surface B_1 will be the convective boundary. The boundaries

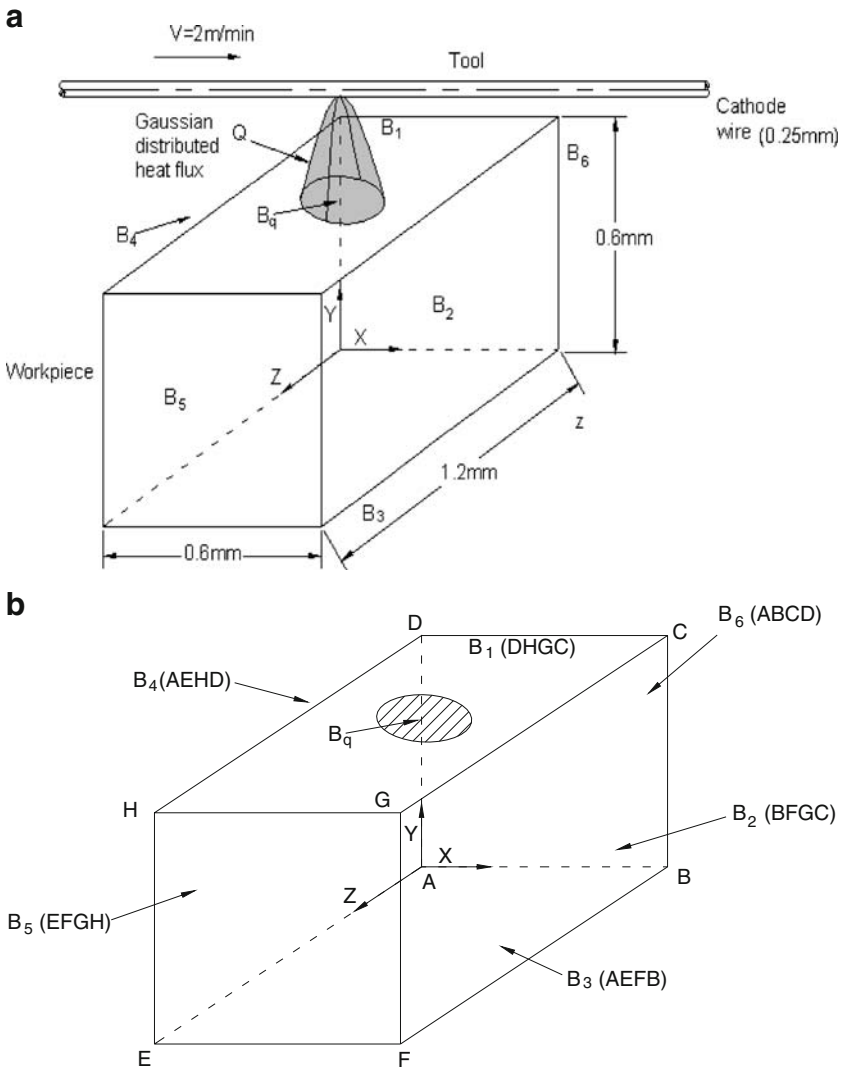

Fig. 2 **a** Geometrical model for TW-ECSM. **b** Computational domain with boundary conditions

B_2 and B_4 are also considered as convective boundaries as it will dissipate heat throughout the computational time, irrespective of on or off time. Hence, we can write,

$$q_c = h(T - T_0) \text{ on } B_1 - B_q,\ B_2,\ \text{and } B_4 \text{ for } t > 0 \tag{5}$$

where h is convective heat transfer coefficient of the electrolyte ($W/m^2{-}K$) in which workpiece is completely dipped.

3 Finite element formulation

The Galerkin's finite element formulation [21] has been applied to obtain the temperature distribution within the computational domain (Fig. 2b). The following expressions are obtained, when Galerkin's method is applied to Eqs. 1–5.

$$\left.\begin{aligned} [K]^e &= \int_{D^e} k[B]^{eT}[B]^e dD^e \\ [K]^b &= \int_{B_h} h\{N\}^b\{N\}^{bT} dB_h \\ [C]^e &= \int_{D^e} \rho C_p\{N\}^e\{N\}^{eT} dD^e \\ \{f_c\}^b &= \int_{B_h} T_0 h\{N\}^b dB_h \\ \{f_q\}^b &= \int_{B_q} \{N\}^b q_w dB_q \end{aligned}\right\}. \tag{6}$$

Here, $[B]^e$ is the matrix of derivatives of nodal interpolation functions for typical area element. B_h is the convective boundaries ($B_1{-}B_q$, B_2, and B_4) and B_q is boundary of input heat flux. The Gauss quadrature technique is used to evaluate elemental matrices and

vectors. The assembled equation for whole workpiece domain can be written as:

$$[\mathrm{GC}]_{nnm \times nnm}\left\{\dot{T}\right\}_{nnm \times 1} + [\mathrm{GK}]_{nnm \times nnm}\{T\}_{nnm \times 1} = \{\mathrm{GF}\}_{nnm \times nnm} \quad (7)$$

where [GC] is the global capacitance matrix, [GK] is the global stiffness matrix, {GF} is the global right side force vector, $\{T\}$ is global temperature vector, and $\left\{\dot{T}\right\}$ is time derivative of $\{T\}$. Equation 7 represents a set of ordinary differential equations in the variable $\{T\}$ as a function of time t; these equations are converted to a set of algebraic equations by the application of implicit FDM. Here, the solution marches in time, in steps of Δt until the desired final time is reached. In the present model, Δt is divided into two-time steps Δt_1 and Δt_2. Here, Δt_1 and Δt_2 are pulse on time and off time of the spark, respectively.

4 Results and discussion

4.1 Calculation of MRR

For calculation of MRR from the workpiece during TW-ECSM, it is assumed that the discharge occurs only along the axis of the wire and only one discharge occurs at any instant. Also, it is considered that no consecutive sparks occur at the same location. The cathode wire is considered to move along the X-axis at Z=0.6 mm on top surface (X–Z plane) of the workpiece (Fig. 2). The velocity of the wire (V_w) is taken as 2 m/min [1]. Total distance traveled by the wire across the workpiece is 0.6 mm (from X=0 to X=0.6 mm). On time and off time of the spark are taken as 500 and 100 μs, respectively. So, total pulse duration is 600 μs. Hence, time required to travel across the workpiece width (0.6 mm) is calculated as 18,000 μs. During this duration, 30 numbers of sparks are possible. This requires a discretized domain of at least 30 locations on which sparking can occur. It is assumed that the sparks occurring at a place do not overlap and the sparks should fall completely on the top surface of the domain as shown in Fig. 3. Hence, for 30-spark locations, a domain having nodes more than 4,500 is required. The present computing machine available is not capable to perform calculations with array size more than 4,500×4,500. Due to this limitation, wire travel distance across the workpiece is not considered for 0.6 mm. Instead, MRR is calculated based on only computational time of 1,200 μs when wire travels a distance of 0.04 mm over the workpiece. During this computational time, two sparks are possible. This way, wire velocity has been incorporated in the calculation of MRR.

The location of the first spark is assumed at X=0.15 mm, Z=0.6 mm on top surface (X–Z plane, Y=0.6 mm) as shown in Fig. 3. The nodal values of input heat flux for the boundary elements on the top surface of workpiece is the function of radius from the center of axis of the spark as given by Eq. 4. Using the global coordinates of each node of the boundary element, the distance from the axis of the spark is calculated. The distance of each node of a boundary element is compared with the radius of spark. If distance of at least one node of a boundary element is less than the radius of the spark or if the distance of at least two nodes of a boundary element are equal to distance of radius

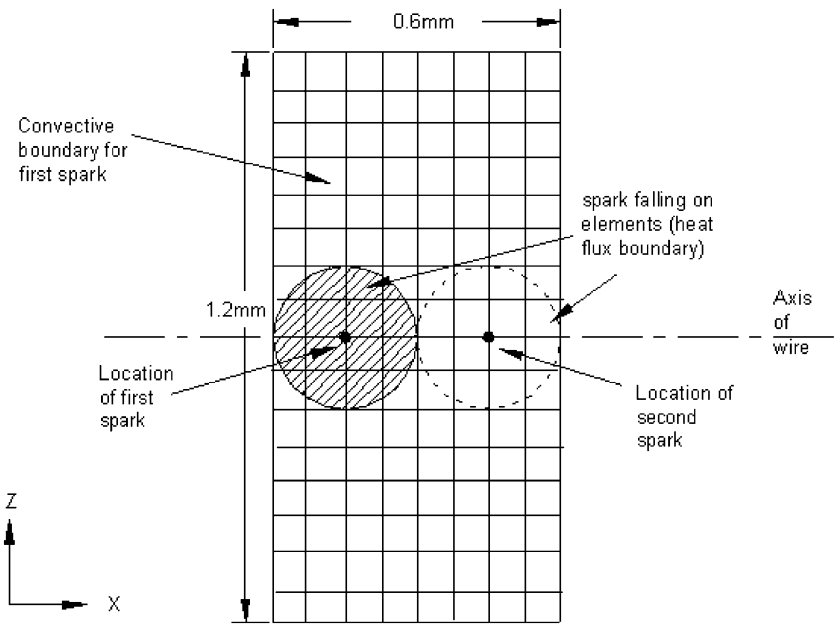

Fig. 3 Location of two sparks on X–Z plane at Y=0.6 mm

of spark, the element is taken as incoming heat flux boundary, else the element is taken as convective boundary element. This logic is incorporated in the developed software. So, when the location and radius of the spark is specified, the software can locate the incoming heat flux boundary elements and convective boundary elements on the top surface of the workpiece.

After the on time of the first spark, an off time of 100 μs is considered. During this period, the whole top surface DHGC (Fig. 2) will be considered as convective boundary. The second spark is assumed at X=0.45 mm, Z=0.6 mm on X–Z plane at Y=0.6 mm as shown in Fig. 3. The temperature distribution in the workpiece domain at the end of the first pulse duration is used as the initial temperature for the calculation of nodal temperature for the second pulse duration.

Contour plots of temperature at the top surface of the workpiece after the first and second spark at X=0.15 mm and X=0.45 mm are shown in Fig. 4. Figure 4a, b shows the contour plots after first and second sparks, respectively. Isotherms are also plotted at different X–Y sections (depth direction) of the domain for different voltage and machining current. The isotherms in X–Y plane at Z=0.6 mm for 20 V and 25 A input power are shown in Fig. 5. Isotherms in X–Y plane after the first and second spark are shown in Fig. 5a, b, respectively. The volume of the material melted is computed by generating the isotherms for the temperature equal to and above the melting temperature (T_m) of the workpiece material. This is done by interpolating the nodal temperatures on the top surface as well as in the depth direction of the workpiece. The isotherms in Figs. 4 and 5 show the crater formed in the workpiece material. The volume of the crater formed is calculated by assuming its shape to be of hemi-ellipsoid. The volume V of a hemi-ellipsoid is given by, $V = \frac{2}{3} \times \pi \times a \times b \times c$ where a, b, and c are the half axes of the ellipsoid [5].

Initially, the MS workpiece is at the room temperature (20°C). When the workpiece is subjected to the first spark, the temperature of the workpiece increases. At the end of the first spark, the volume of material having temperature more than the melting temperature (1,150°C) of MS are removed from the workpiece. The remaining workpiece material will be at a higher temperature than the room temperature. These temperatures are stored to use as initial temperature of the workpiece for calculation of nodal temperature in the workpiece due to second spark. The volume after the first spark and the volume removed by the second spark are added to get the total volume of material removed due to two sparks, i.e., total duration of two sparks are 2×600 μs. MRR is then calculated using Eq. 8.

$$MRR = \frac{(V_1 + V_2) \times 60}{(t_{p1} + t_{p2}) \times 10^{-6}} mm^3/\text{min}$$

V_1 Volume of material removed after first spark (mm^3)
V_2 Volume of material removed after second spark (mm^3)
t_{p1} First pulse duration (μs)
t_{p2} Second pulse duration (μs)

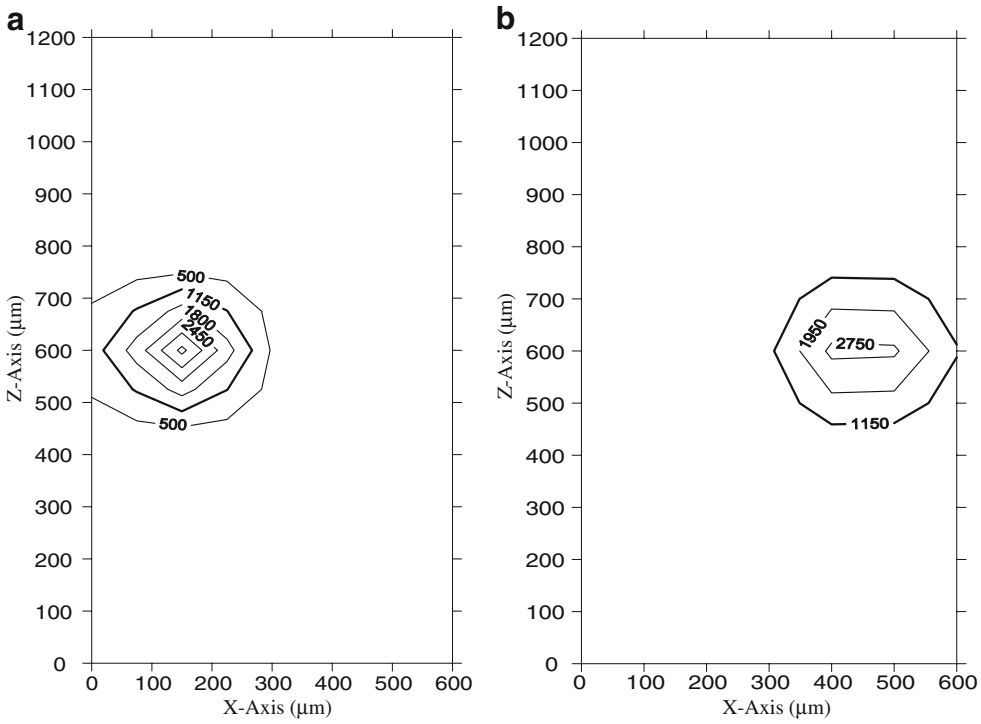

Fig. 4 Contour plots on X–Z plane at Y=0.6 mm for 20 V and 25 A input power supply **a** after first spark at location X=0.15 mm, Z=0.6 mm and **b** after second spark at location X=0.45 mm, Z=0.6 mm

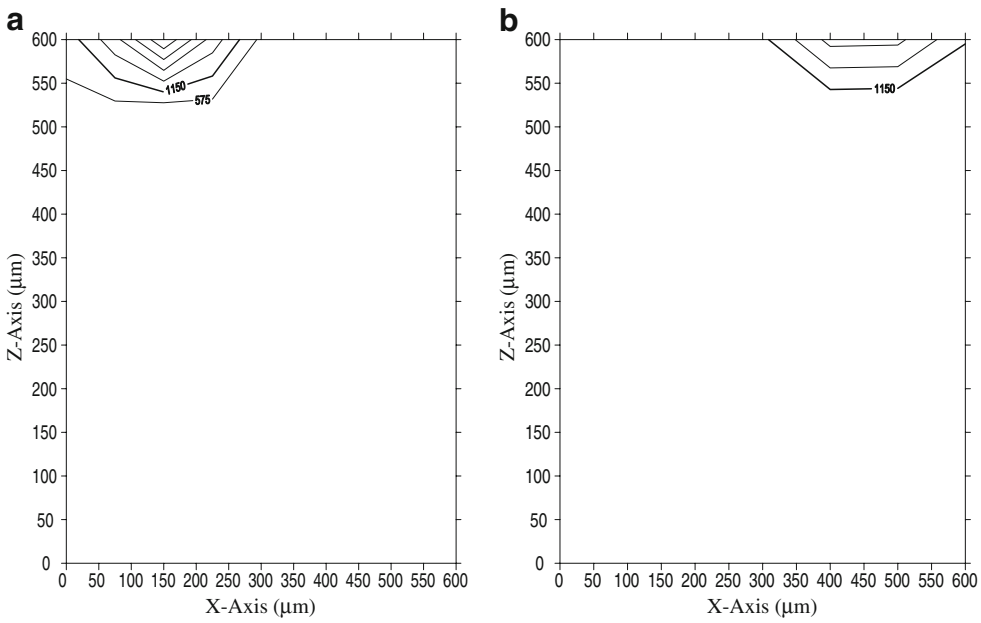

Fig. 5 Contour plots on X–Y plane at Z=0.6 mm for 20 V and 25 A input power supply **a** after first spark at location X=0.15 mm, Y=0.6 mm and **b** after second spark at location X=0.45 mm, Y=0.6 mm

since t_{p1} is taken same as $t_{p2}\left(t_{p1} = t_{p2}\right)$, hence

$$MRR = \frac{(V_1 + V_2) \times 60}{2 \times t_{p1} \times 10^{-6}} mm^3/\text{min}. \quad (8)$$

4.2 Comparison of MRR

McGeough and El Hofy [1] experimentally measured MRR from MS workpiece during TW-ECSM. In their experiment, a copper wire of 0.25 mm diameter was used as cathode electrode moving with a velocity of 2 m/min. The thickness of MS workpiece was 12 mm. The $NaNO_3$ electrolyte, with a 200-g/l solution at 20°C, was used. Each experiment was lasted for about 6 to 12 min, during which current and voltage were recorded on a coulomb counter and oscilloscope, respectively.

The aforementioned problem is solved using the present model for determination of MRR from MS workpiece during TW-ECSM. The workpiece material and cutting conditions used are taken same as used in the literature [1]. The material properties of mild steel are taken from [22]. The domain size has been changed from $12 \times 6 \times 6$ to $1.2 \times 0.6 \times 0.6$mm because of computational limitations of our computing system. The workpiece domain is discretized into eight noded hexahedral elements. Convergence conditions were carried out by increasing the number of elements in the mesh. The simulation showed that the nodal temperature of workpiece domain obtained were essentially unchanged, when the mesh size is in excess of 1,024 elements. The mesh of 1,024 elements is thus found to be adequate for convergence. Hence, the mesh consisting of 1,024 number of square elements each of length 0.075 mm and total 1,377 nodes are used for further analysis. The nodal temperature distribution of the workpiece domain is found using computer with Pentium 4 processor.

MRR is calculated for different supply voltage and machining current. MRR calculated using the present FEM-based model is compared with experimental values obtained by McGeough and El Hofy [1]. The results obtained using the present model shows (Fig. 6) similar pattern as given in literature [1]. MRR calculated using the present FEM-based model increases with increase in voltage. MRR also increases with the increase in feed rate. Calculated MRR at feed rate of 10 mm^2/min and supply voltage of 15 V using the present FEM-based model is found as 38.58 mm^3/min whereas the experimental value of

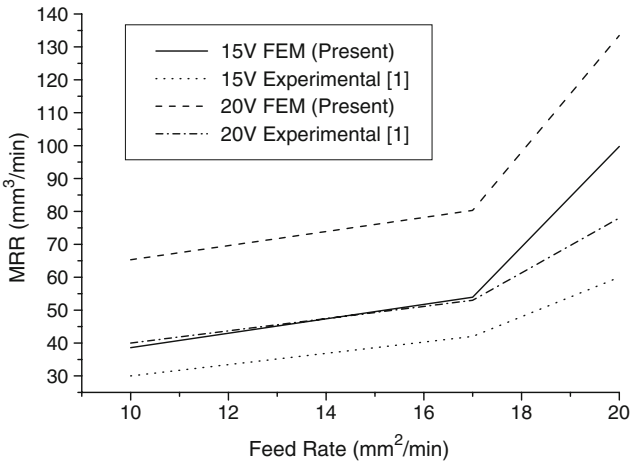

Fig. 6 Variation of MRR with feed rate for different voltage

MRR for the same input condition is 30 mm^3/min. Further, when the feed rate is taken 10 mm^2/min and supply voltage 20 V, the MRR calculated using the present FEM-based model is found 65.33 mm^3/min whereas experimental value is 40 mm^3/min.

Hence, it is observed that MRR calculated using the present model is greater than experimental values. This may be due to the value considered for ejection efficiency during TW-ECSM process. In the present model, the ejection efficiency is assumed to be 100% (it is assumed that all the material, which is melted, is removed). In real situation, some part of the molten material is not completely removed but it adheres back (resolidify) to the parent material because of the quenching effect caused by liquid electrolyte. This plays a dominant role, as the ejection efficiency in TW-ECSM is very low. It may be as low as 10% or even lower than that [12]. Further, there is no exact data available regarding energy partition and spark radius for the combination of MS workpiece, $NaNO_3$ electrolyte, and Cu traveling wire. Also, shape of the crater formed is assumed as hemi-ellipsoid and approximations are done in the calculation of volume during interpolation of coordinates of isotherms. Above-described reasons are responsible for getting different values of computational and experimental results.

4.3 Computational experiments

There is no exact data available regarding energy partition (F_w) and spark radius (R) in TW-ECSM process. Hence, computational experiments have been performed to determine the values of energy partition and spark radius under different operating conditions. Mild steel is taken as workpiece material and mathematical modeling as discussed in Section 2 is used for the computational experiments. The dimension of workpiece taken is 0.6 × 0.6 × 1.2mm. The workpiece is assumed to be submerged 2 mm inside the $NaNO_3$ electrolyte. The diameter of cathode wire (tool) is taken as 0.25 mm and velocity of wire (V_w) as 2 m/min. When the wire travels a distance of 0.04 mm, with 2 m/min, there will be two sparks on the top surface of the workpiece (X–Z plane at Y=0.6 mm).

4.3.1 Energy partition (F_w)

Energy partition is the fraction of the total heat energy effectively utilized for material removal. Taking different values of this energy partition (F_w) in Eq. 4, *MRR* is computed by the procedure as discussed in Section 4.1. Figure 7 shows the best fit curves of energy partition vs. MRR at different values of supply voltage and current. In all these cases, it is seen that by increasing the energy partition, the computational MRR increases. The equation

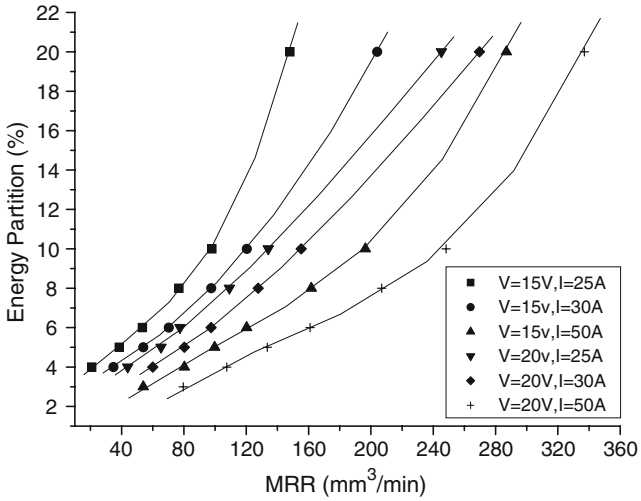

Fig. 7 Variation of energy partition vs. MRR for different values of supply voltage and current

of best fit curve for a supply voltage of 15 V and current of 25 A is obtained as:

$$F_w = 2.37221 + 0.08725(\mathrm{MRR}) - 6.69757 \times 10^{-4}(\mathrm{MRR})^2 + 5.97659 \times 10^{-6}(\mathrm{MRR})^3. \quad (9)$$

Since the experimental value of MRR is 30 mm^3/min for a supply voltage of 15 V and current of 25 A [1], putting this value of MRR in Eq. 9, it is found that F_w is 4.5%. Similarly, F_w is computed for different values of supply voltage and current and shown in Table 1. From Table 1, it is observed that as the input power (VI) increases, the energy partition decreases.

4.3.2 Spark radius (R)

In case of TW-ECSM, material is mainly removed by thermal phenomena. So spark radius is an important parameter in this machining process. But no literature is available regarding the spark radius for TW-ECSM process. In this work, computational experiments have been performed to determine the spark radius for different input power.

Table 1 Computational energy partition for different values of supply voltage and current

Voltage (V)	Current (A)	Ejection efficiency (%)	Spark radius (μm)	Experimental MRR (mm^3/min)	Calculated energy partition (%)
15	25	100	150	30	4.5
15	30	100	150	42	4.3
15	50	100	150	60	3.2
20	25	100	150	40	3.8
20	30	100	150	53	3.7
20	50	100	150	78	2.8

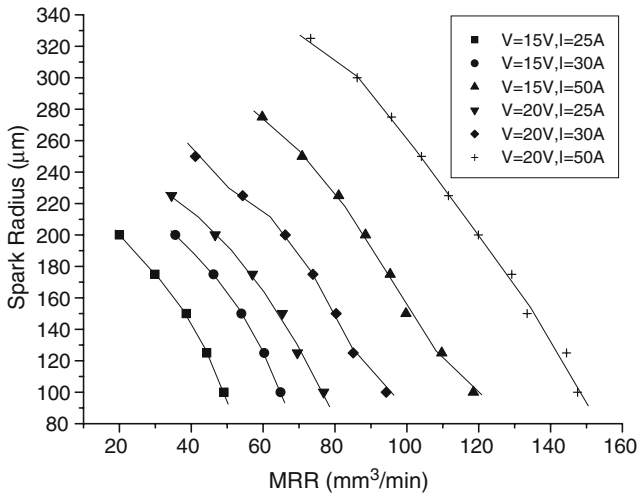

Fig. 8 Variation of spark radius vs. MRR for different values of supply voltage and current

Taking different values of spark radius (R) in Eq. 4, MRR is computed by the procedure as discussed in Section 4.1. Figure 8 shows the best fit curves of spark radius vs. MRR at different values of supply voltage and current. In all these cases, it is seen that by increasing the spark radius the computational MRR decreases. The equation of best fit curve for a supply voltage of 20 V and current of 30 A is obtained as:

$$R = 1442.53714 - 76.99223(\mathrm{MRR}) + 1.83453(\mathrm{MRR})^2 - 0.01919(\mathrm{MRR})^3 + 7.20722 \times 10^{-5}(\mathrm{MRR})^4. \quad (10)$$

Since the experimental value of MRR is 53 mm^3/min for a supply voltage of 20 V and current of 30 A [1], putting this value of MRR in Eq. 10, it is found that R is 226.88 μm. Similarly, for different values of supply voltage and current, R is computed and shown in Table 2. From Table 2, it is observed that as the input power (VI) increases, the spark radius increases.

Table 2 Computational spark radius for different values of supply voltage and current

Voltage (V)	Current (A)	Ejection efficiency (%)	Energy partition (%)	Computational MRR (mm^3/min)	Calculated spark radius (μm)
15	25	100	5	30	174.85
15	30	100	5	42	185.00
15	50	100	5	60	274.89
20	25	100	5	40	215.24
20	30	100	5	53	226.88
20	50	100	5	78	317.86

Table 3 Cutting conditions

Electrolyte	$NaNO_3$
h (W/m^2-K)	20,870
I (A)	25
V_w (m/min)	2
R (μm)	150
F_w	5%
t_{on} (μs)	500
T_0 (K)	293
Supply voltage (V)	20

4.4 Parametric studies: MS workpiece

The influences of process parameters such as energy partition, duty factor, spark radius, and ejection efficiency on MRR and maximum depth of crater formed in the workpiece during TW-ECSM were studied. Mild steel was taken as workpiece material. The cutting conditions are given in Table 3 and material properties of workpiece material are given in Table 4. Governing equation and boundary conditions as discussed in Sections 2.2 and 2.3, respectively, are the same through out the study.

4.4.1 Effect of energy partition

Figure 9a shows the effect of energy partition (F_w) on MRR in TW-ECSM. Here, it is observed that MRR increases with the increase in energy partition. Increase in the energy partition means the amount of heat going to the workpiece is more, which is responsible for larger volume of material melting and hence high MRR.

Effect of energy partition on maximum depth of crater is shown in Fig. 9b. Maximum depth of crater increases with increase in energy partition. When energy partition is 20%, maximum depth of crater observed is 68 μm. Higher value of energy partition means more amount of heat energy penetrating into the workpiece, which results in larger material removal in depth direction.

4.4.2 Effect of duty factor

Duty factor is the ratio of spark on time and pulse duration (on time + off time). Duty factor of 50%, 75%, 83%, 87%, and 90% are taken for the present study by increasing the spark on time from 100 to 900 μs with incremental time of

Table 4 Material properties of mild steel (0.14% C, 0.25% Si, 0.60 Mn)

C_p (J/Kg K)	461
k (W/m^2 K)	50.2
T_m (°C)	1,150
ρ (kg/m^3)	7,870

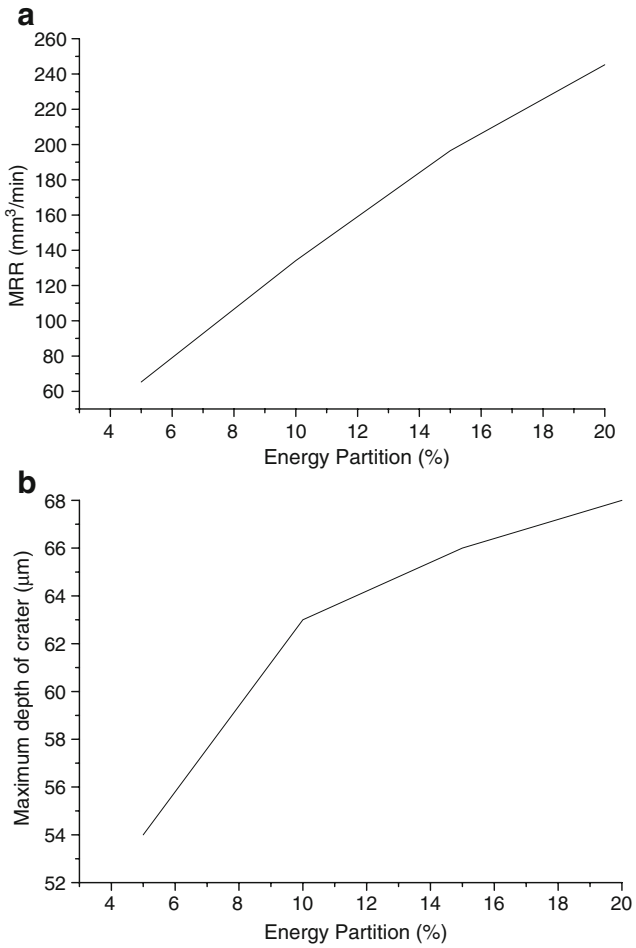

Fig. 9 Effect of energy partition due to TW-ECSM of MS workpiece with voltage=20 V, current=25A, and *df*=83% **a** on MRR and **b** on maximum depth of crater

200 μs keeping off time of 100 μs constant. Figure 10a shows the effect of duty factor on MRR in TW-ECSM. Here, it is observed that MRR increases with the increase in duty factor. With increase in duty factor, the spark energy will be transferred to the workpiece for more time because of which volume of MS material melted is also increased. Hence, the material removal rate is increased with increase in duty factor. Figure 10b shows the effect of duty factor on maximum depth of crater. As the duty factor increases, maximum depth of crater also increases.

4.4.3 Effect of spark radius

The effect of spark radius on MRR is shown in Fig. 11a. Here, it is observed that MRR obtained is 76.83 mm^3/min for spark radius of 100 μm. MRR decreases to 65.33 mm^3/min for spark radius of 150 μm. Further, MRR decreases to 34.52 mm^3/min for spark radius of 225 μm. This shows a decreasing trend of MRR with respect to increase in spark radius. This is because heat flux decreases with increase in spark radius. Due to lower heat flux, less material is melted. Because of this, MRR decreases with increase in spark radius.

Effect of spark radius on maximum depth of crater is shown in Fig. 11b. Maximum depth of crater decreases with increase in spark radius. When spark radius is 100 μm, maximum depth of crater observed is 64 μm. At lower value of spark radius more amount of heat energy penetrating into the workpiece, which results in larger material removal in depth direction.

4.4.4 Effect of ejection efficiency

Ejection efficiency or material removal efficiency is the ratio of actual removal to molten volume of work material. Figure 12 shows the effect of ejection efficiency on MRR. Here, it is observed that with increase in ejection efficiency, material removal rate increases. This is because when ejection efficiency increases, more volume of melted material is removed and less volume of melted material is resolidified. Hence, MRR increases.

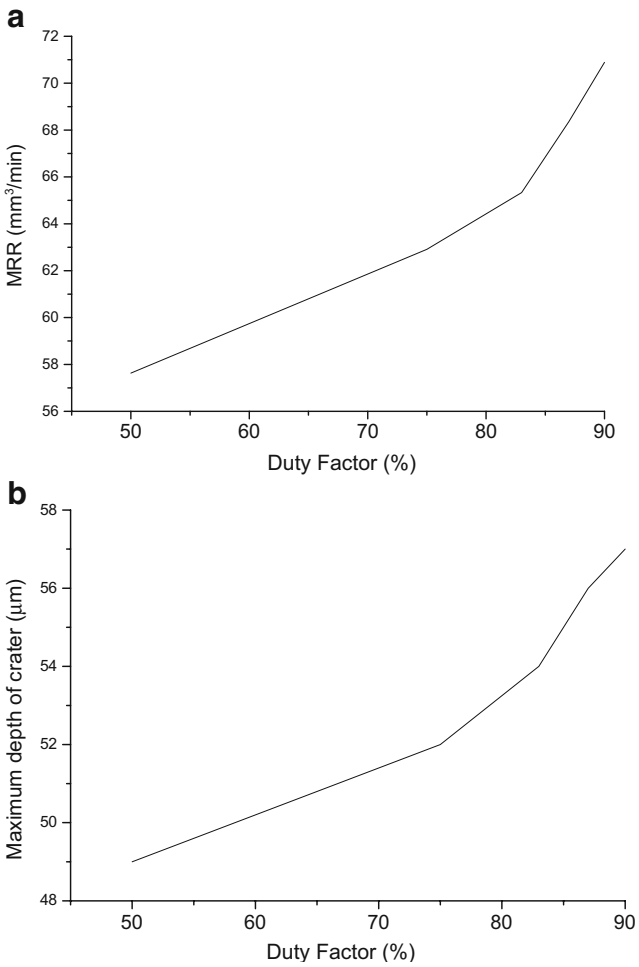

Fig. 10 Effect of duty factor due to TW-ECSM of MS workpiece with voltage=20 V, current=25A, and F_w=5% **a** on MRR and **b** on maximum depth of crater

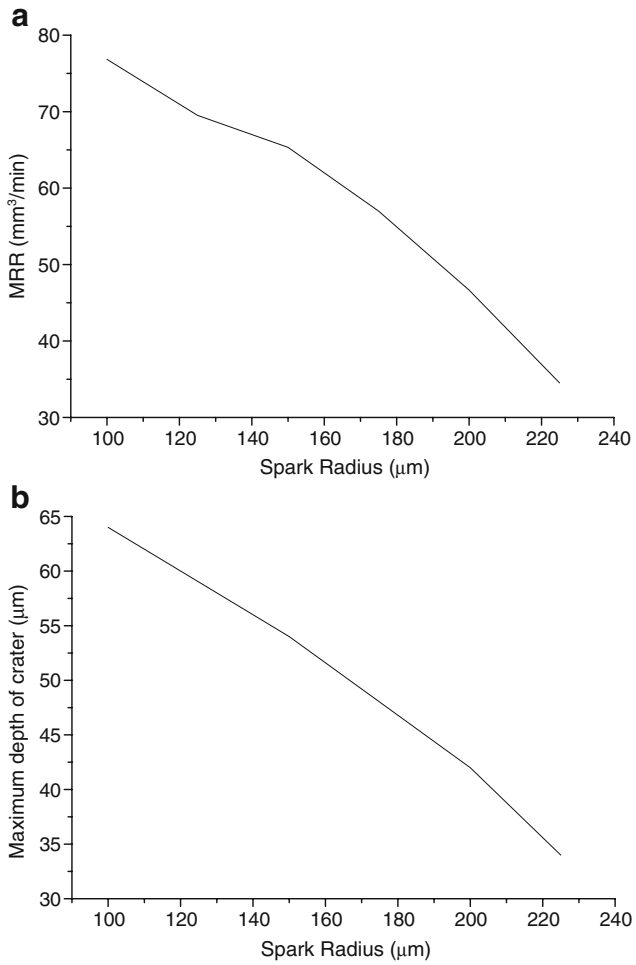

Fig. 11 Effect of spark radius due to TW-ECSM of MS workpiece with voltage=20 V, current=25A, *df*=83%, and F_w=5% **a** on MRR and **b** on maximum depth of crater

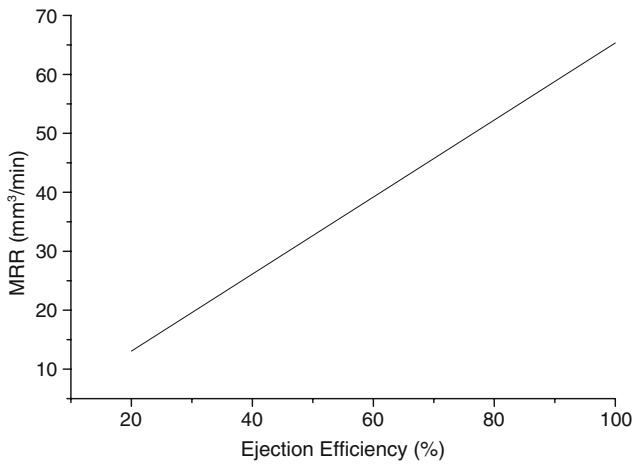

Fig. 12 Effect of ejection efficiency on MRR due to TW-ECSM of MS workpiece with voltage=20 V, current=25A, *df*=83%, and F_w=5%

Table 5 Material properties of glass

C_p (J/Kg K)	750
k (W/m^2 K)	1.14
T_m (°C)	820
ρ (kg/m^3)	2,230

4.5 Parametric studies: glass workpiece

The effect of process parameters such as energy partition, duty factor, spark radius, and ejection efficiency on MRR and maximum depth of crater formed in the workpiece during TW-ECSM were studied. Glass was taken as workpiece material. The cutting conditions are given in Table 3 and material properties of workpiece material are given in Table 5. Governing equation and boundary conditions as discussed in Sections 2.2 and 2.3, respectively, are the same through out the study.

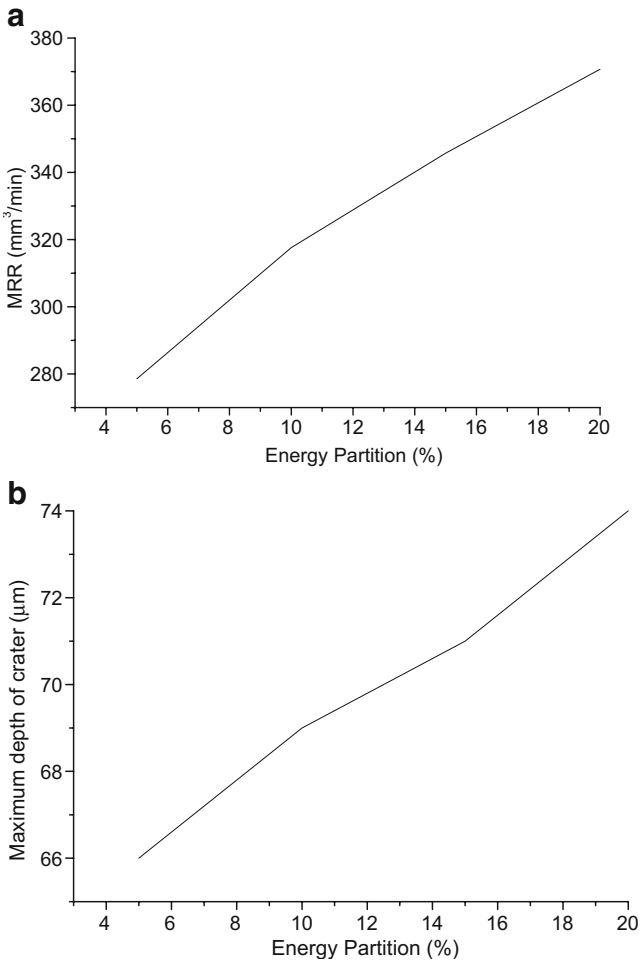

Fig. 13 Effect of energy partition due to TW-ECSM of glass workpiece with voltage=20 V, current=25A, and *df*=83% **a** on MRR and **b** on maximum depth of crater

4.5.1 Effect of energy partition

The effect of energy partition (F_w) on MRR is shown in Fig. 13a. Here, it is observed that MRR obtained is 278.57 mm^3/min for 5% energy partition. MRR increases to 317.61 mm^3/min for energy partition of 10%. Further, MRR increases to 370.69 mm^3/min for energy partition of 20%. This shows an increasing trend of MRR with respect to increase in energy partition. The reason for this increasing trend is same as discussed for MS workpiece.

Effect of energy partition on maximum depth of crater is shown in Fig. 13b. Maximum depth of crater increases with increase in energy partition. When energy partition is 20%, maximum depth of crater observed is 74 μm. Higher value of energy partition means more amount of heat energy penetrating into the workpiece, which results in larger material removal in depth direction.

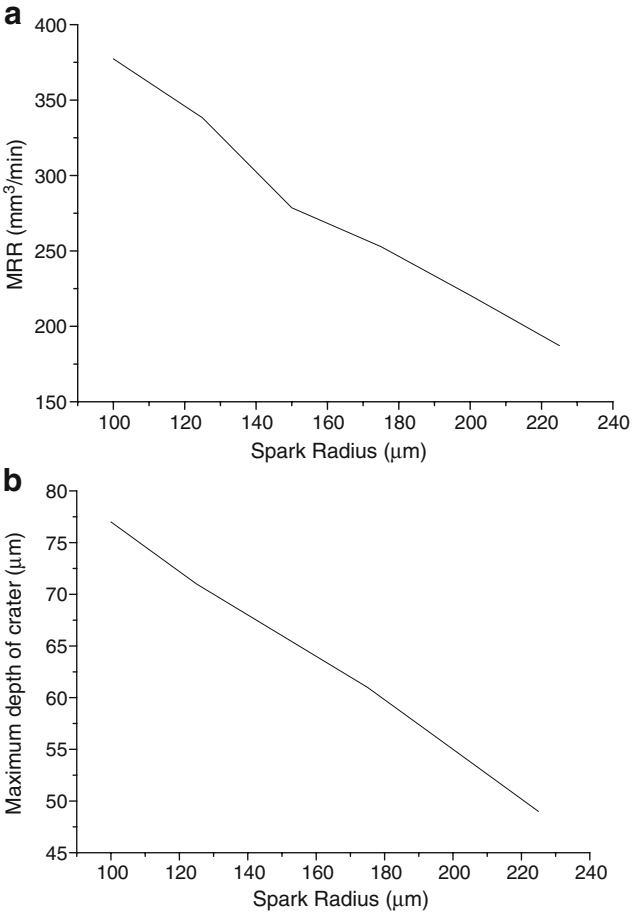

Fig. 15 Effect of spark radius due to TW-ECSM of glass workpiece with voltage=20 V, current=25A, *df*=83%, and F_w=5% **a** on MRR and **b** on maximum depth of crater

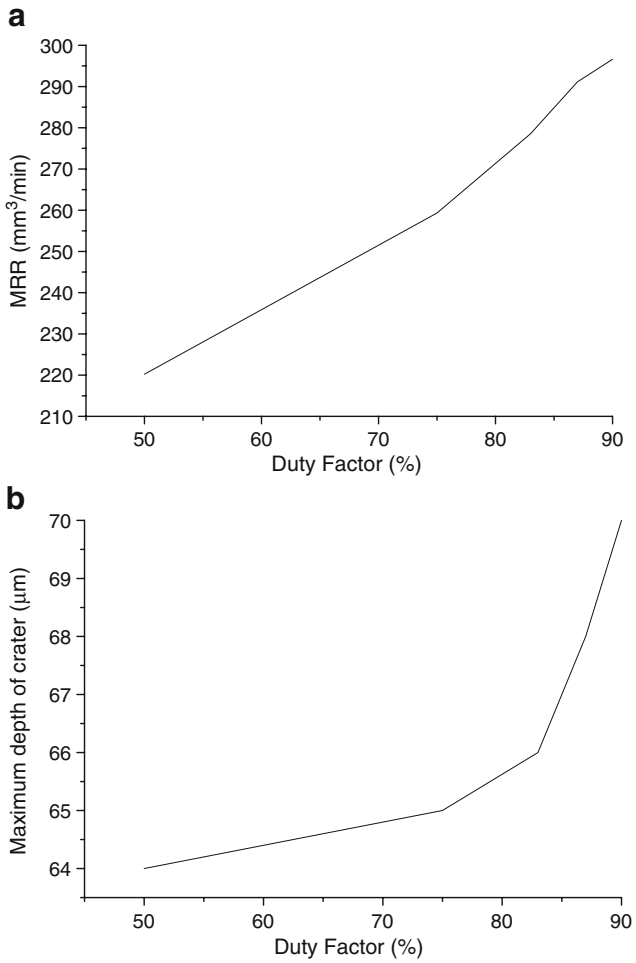

Fig. 14 Effect of duty factor due to TW-ECSM of glass workpiece with voltage=20 V, current=25A, and F_w=5% **a** on MRR and **b** on maximum depth of crater

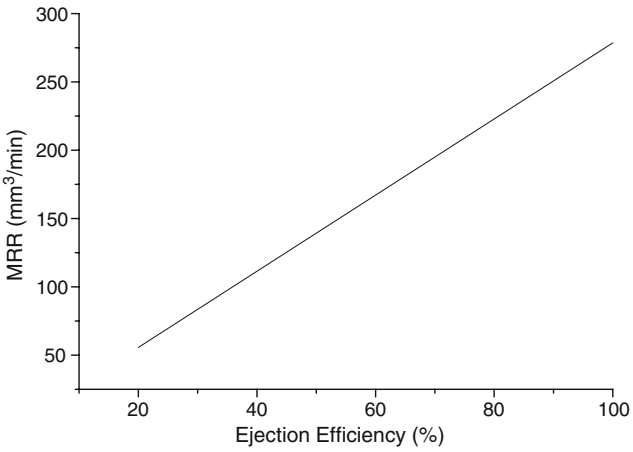

Fig. 16 Effect of ejection efficiency on material removal rate due to TW-ECSM of glass workpiece with voltage=20 V, current=25A, *df*=83%, and F_w=5%

4.5.2 Effect of duty factor

Glass workpiece is undertaken with the same duty factor as those used for MS workpiece. Figure 14a shows the effect of duty factor on MRR in TW-ECSM. Here, it is observed that MRR increases with the increase in duty factor. The reason is again same that with the increase in duty factor, pulse on time increases, and hence, the spark energy will be transferred to the workpiece for more time, because of which more volume of material is melted, and hence, MRR increases. However, for all values of duty factor, the MRR is higher in case of glass workpiece than MS workpiece. This is because melting temperature of glass is lower compared with MS. Figure 14b shows the effect of duty factor on maximum depth of crater. As the duty factor increases, maximum depth of crater also increases.

4.5.3 Effect of spark radius

The effect of spark radius on MRR is shown in Fig. 15a. Here, it is observed that MRR obtained is 377.36 mm^3/min for spark radius of 100 μm. MRR decreases to 278.57 mm^3/min for spark radius of 150 μm. Further, MRR decreases to 187.26 mm^3/min for spark radius of 225 μm. This shows a decreasing trend of MRR with respect to increase in spark radius. The reason for this decreasing trend is same as discussed for MS workpiece. Effect of spark radius on maximum depth of crater is shown in Fig. 15b. Maximum depth of crater decreases with increase in spark radius.

4.5.4 Effect of ejection efficiency

Figure 16 shows the effect of ejection efficiency on MRR. Here, it is observed that MRR obtained is 55.71 mm^3/min for ejection efficiency of 20%. MRR increases to 167.14 mm^3/min for ejection efficiency of 60%. Further, MRR increases to 278.57 mm^3/min for ejection efficiency of 100%. This shows an increasing trend of MRR with respect to increase in ejection efficiency. The reason for this increasing trend is that when ejection efficiency increases, more volume of melted material is removed, and hence, MRR increases.

From the above study, it is seen that MRR during TW-ECSM process is influenced by four interacting parameters, viz., energy partition, spark radius, duty factor, and ejection efficiency. It seems that a complex nonlinear relationship exists between these parameters and MRR. Hence, it is quite difficult to select the optimum parameters for specific application of TW-ECSM process. To overcome this difficulty, it is suggested by the authors that the results obtained from the present FEM model can be further used to develop a soft computing-based comprehensive TW-ECSM process model to select the optimum parameters for specific application of TW-ECSM process.

5 Conclusions

In the present work, a 3-D finite element transient thermal model has been developed to estimate the temperature field and MRR due to Gaussian distributed input heat flux of a spark during TW-ECSM. Computational experiments have been performed to determine energy partition and spark radius. The present model is applied to two types of workpiece materials, MS and glass, to study the influence of different input parameters such as energy partition, duty factor, spark radius, and ejection efficiency on MRR. Some of the conclusions from the study are summarized below:

1. The material removal rate obtained using the present model from MS workpiece is found to be more when compared with the experimental results. It is because in the present model, ejection efficiency is assumed to be 100% and there is no exact data available regarding energy partition and spark radius.
2. Energy partition is found to decrease with increase in input power whereas spark radius is found to increase with increase in input power.
3. With increase in energy partition (F_w), MRR and depth of crater increases for both MS and glass workpiece material.
4. For both MS and glass workpiece material with increase in duty factor, the volume of material melted is increased. Hence, the material removal rate is increased with increase in duty factor. Similar trend is observed for maximum depth of crater with increase in duty factor.
5. MRR decreases with the increase in spark radius during TW-ECSM for both MS and glass workpiece material.
6. MRR increases with the increase in ejection efficiency during TW-ECSM for both MS and glass workpiece material.

References

1. McGeough JA, El Hofy H (1988) Evaluation of an apparatus for electrochemical arc wire-machining. J Eng Ind 110:119–123
2. Kurafuji H, Suda K (1968) Electrical discharge drilling of glass. Ann CIRP 16:415–419
3. Wuthrich R, Fascio V (2005) Machining of non-conducting materials using electrochemical discharge phenomenon-an overview. Int J Mach Tools Manuf 45:1095–1108. doi:10.1016/j.ijmachtools.2004.11.011
4. Basak I, Ghosh A (1996) Mechanism of spark generation during electrochemical discharge machining: a theoretical model and

experimental investigation. J Mater Process Technol 62:46–53. doi:10.1016/0924-0136(95)02202-3
5. Jain VK, Dixit PM, Pandey PM (1999) On the analysis of the electro chemical spark machining process. Int J Mach Tools Manuf 39:165–186. doi:10.1016/S0890-6955(98)00010-8
6. Kulkarni A, Sharan R, Lal GK (2002) An experimental study of discharge mechanism in electrochemical discharge machining. Int J Mach Tools Manuf 42:1121–1127. doi:10.1016/S0890-6955(02)00058-5
7. Wuthrich R, Bleuler H (2004) A model for electrode effects using percolation theory. Electrochim Acta 49:1547–1554
8. Yerokhin AI, Nie X, Leyland A, Maetthews A, Dowey SJ (1999) Plasma electrolysis for surface engineering. Surf Coat Tech 122:73–93. doi:10.1016/S0257-8972(99)00441-7
9. Vogt H (1999) The anode effect as a fluid dynamic problem. J Appl Electrochem 29:137–145. doi:10.1023/A:1003477004486
10. Fascio V, Wuthrich R, Bleuler H (2004) Spark assisted chemical engraving in the light of electrochemistry. Electrochim Acta 49:3997–4003. doi:10.1016/j.electacta.2003.12.062
11. Wuthrich R, Hof LA, Lal A, Fujisaki K, Bleuler H, Mandin P, Picard G (2005) Physical principles and miniaturization of spark assisted chemical engraving (SACE). J Micromech Microeng 15:268–275. doi:10.1088/0960-1317/15/10/S03
12. Jain VK, Rao PS, Choudhury SK, Rajurkar KP (1991) Experimental investigations into traveling wire electrochemical spark machining (TW-ECSM) of composites. J Eng Ind 113:75–84
13. Singh YP, Jain VK, Kumar P, Agrawal DC (1996) Machining piezoelectric (PZT) ceramics using an electrochemical spark machining (ECSM) process. J Mater Process Technol 58:24–31. doi:10.1016/0924-0136(95)02102-7
14. Peng WY, Liao YS (2004) Study of electrochemical discharge machining technology for slicing non-conductive brittle materials. J Mater Process Technol 149:363–369. doi:10.1016/j.jmatprotec.2003.11.054
15. Nesarikar VV, Jain VK, Choudhury SK (1994) Traveling wire electrochemical spark machining of thick sheets of Kevlar–epoxy composites. Proceedings of the Sixteenth AIMTDR Conference, pp 672–677
16. Basak I, Ghosh A (1997) Mechanism of material removal in electrochemical discharge machining: a theoretical model and experimental verification. J Mater Process Technol 71:350–359. doi:10.1016/S0924-0136(97)00097-6
17. Bhondwe KL, Yadava V, Kathiresan G (2006) Finite element prediction of material removal rate due to electrochemical spark machining. Int J Mach Tools Manuf 46:1699–1706. doi:10.1016/j.ijmachtools.2005.12.005
18. Prasad BVSSS, Mishra PK, Banerjee S (1997) Analysis of three-dimensional transient heat conduction for predicting wire erosion in the wire electrical discharge machining process. J Mater Process Technol 65:134–142. doi:10.1016/0924-0136(95)02253-8
19. Hargrove SK, Ding D (2007) Determining cutting parameters in wire EDM based on workpiece surface temperature distribution. Int J Adv Manuf Technol 34:295–299. doi:10.1007/s00170-006-0609-0
20. Venkatashan SP (2004) First course in heat transfer. Ane Books, New Delhi
21. Reddy JN (2005) An introduction to finite element method, 3rd edn. McGraw-Hill, New Delhi
22. Nayar A (2002) The steel hand book. McGraw-Hill, New Delhi